Article

Measurement of $^{19}\mathrm{F}(p,\ \gamma)^{20}\mathrm{Ne}$ reaction suggests CNO breakout in first stars

https://doi.org/10.1038/s41586-022-05230-x

Received: 28 February 2022

Accepted: 11 August 2022

Liyong Zhang[1], Jianjun He[1]✉, Richard J. deBoer[2], Michael Wiescher[2]✉, Alexander Heger[3], David Kahl[4], Jun Su[1], Daniel Odell[5], Yinji Chen[1], Xinyue Li[1], Jianguo Wang[6], Long Zhang[7], Fuqiang Cao[7], Hao Zhang[1], Zhicheng Zhang[8], Xinzhi Jiang[1], Luohuan Wang[1], Ziming Li[1], Luyang Song[1], Hongwei Zhao[6], Liangting Sun[6], Qi Wu[6], Jiaqing Li[6], Baoqun Cui[7], Lihua Chen[7], Ruigang Ma[7], Ertao Li[8], Gang Lian[7], Yaode Sheng[1], Zhihong Li[7], Bing Guo[7], Xiaohong Zhou[6], Yuhu Zhang[6], Hushan Xu[6], Jianping Cheng[1] & Weiping Liu[7,9]✉

Proposed mechanisms for the production of calcium in the first stars (population III stars)—primordial stars that formed out of the matter of the Big Bang—are at odds with observations[1]. Advanced nuclear burning and supernovae were thought to be the dominant source of the calcium production seen in all stars[2]. Here we suggest a qualitatively different path to calcium production through breakout from the 'warm' carbon–nitrogen–oxygen (CNO) cycle through a direct experimental measurement of the $^{19}\mathrm{F}(p,\gamma)^{20}\mathrm{Ne}$ breakout reaction down to a very low energy point of 186 kiloelectronvolts, reporting a key resonance at 225 kiloelectronvolts. In the domain of astrophysical interest[2], at around 0.1 gigakelvin, this thermonuclear $^{19}\mathrm{F}(p,\gamma)^{20}\mathrm{Ne}$ rate is up to a factor of 7.4 larger than the previous recommended rate[3]. Our stellar models show a stronger breakout during stellar hydrogen burning than previously thought[1,4,5], and may reveal the nature of calcium production in population III stars imprinted on the oldest known ultra-iron-poor star, SMSS0313-6708[6]. Our experimental result was obtained in the China JinPing Underground Laboratory[7], which offers an environment with an extremely low cosmic-ray-induced background[8]. Our rate showcases the effect that faint population III star supernovae can have on the nucleosynthesis observed in the oldest known stars and first galaxies, which are key mission targets of the James Webb Space Telescope[9].

Stars are the nuclear forges of the cosmos, responsible for the creation of most elements heavier than helium in the Universe. Some of these elements are created in the hearts of stars over the course of billions of years, whereas others are formed in just a few seconds during the explosive deaths of massive stars. These heavy elements have an important role in the Universe, enabling the formation of complex molecules and dust, which facilitate the cooling and condensation of molecular clouds, aiding the formation of new stars like our Sun. The first generation of stars, called population III (pop III) stars or primordial stars, formed from the pristine matter left by the Big Bang, thus play a special part in seeding the Universe with the first heavy elements and creating suitable conditions for future generations of stars and galaxies.

Every star, regardless of its mass, spends the majority of its life quiescently fusing hydrogen into helium in its core through two primary mechanisms: p–p chains and catalytic carbon–nitrogen–oxygen (CNO) cycles[10–12]. Which mechanism dominates hydrogen burning is determined by the temperature in the core of a star. In stars with initial masses less than approximately 1.2 solar masses ($M_\odot$), with relatively cool cores ($T \leq 0.02$ GK), the p–p chains dominate the hydrogen fusion, whereas in stars with higher initial masses and hotter cores, the CNO cycles take over. As a catalytic reaction, the total number of CNO nuclei remains constant, unless a breakout reaction sequence causes a leakage toward the NeNa mass region, or if temperature and density are high enough to forge new carbon by the triple-alpha (3α) process. The latter two occur in primordial massive stars. The only reaction that can potentially remove the catalytic material from the cycle at lower temperatures is the fusion of ^{19}F with a proton to form ^{20}Ne, denoted $^{19}\mathrm{F}(p,\gamma)^{20}\mathrm{Ne}$ (ref. [13]). Previously, this reaction was thought to be weak compared to the competing $^{19}\mathrm{F}(p,\alpha)^{16}\mathrm{O}$ reaction, so most of the ^{19}F produced by the CNO cycle would be recycled back into ^{16}O, with no substantial chemical abundance changes[4].

The most metal-poor stars observed in the Milky Way's halo today display the diluted nucleosynthetic signatures resulting from pop III stars that preceded them[14]. A previous work[6] discovered one of the

---

[1]Key Laboratory of Beam Technology of Ministry of Education, College of Nuclear Science and Technology, Beijing Normal University, Beijing, China. [2]Nuclear Science Laboratory, University of Notre Dame, Notre Dame, IN, USA. [3]School of Physics and Astronomy, Monash University, Victoria, Australia. [4]Extreme Light Infrastructure – Nuclear Physics, Horia Hulubei National Institute for R&D in Physics and Nuclear Engineering (IFIN-HH), Bucharest-Măgurele, Romania. [5]Institute of Nuclear and Particle Physics and Department of Physics and Astronomy, Ohio University, Athens, OH, USA. [6]Institute of Modern Physics, Chinese Academy of Sciences, Lanzhou, China. [7]China Institute of Atomic Energy, Beijing, China. [8]College of Physics and Optoelectronic Engineering, Shenzhen University, Shenzhen, China. [9]College of Science, Southern University of Science and Technology, Shenzhen, China. ✉e-mail: hejianjun@bnu.edu.cn; michael.c.wiescher.1@nd.edu; wpliu@ciae.ac.cn

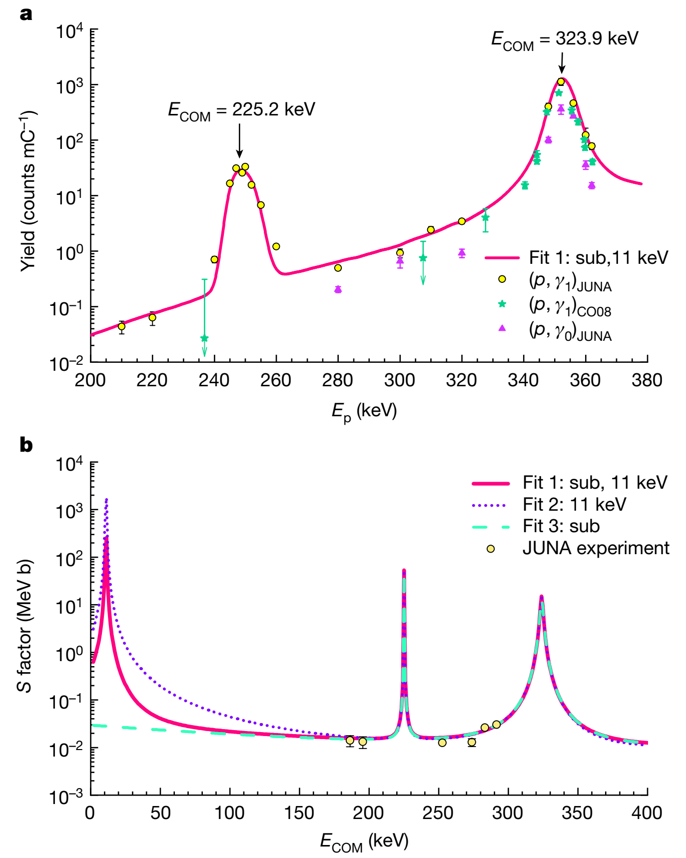

Fig. 1 | Experimental results of the $^{19}F(p, \gamma)^{20}Ne$ reaction. a, Experimental yields of the $^{19}F(p, \gamma_{0,1})^{20}Ne$ reaction measured at JUNA. Previous experimental (p, γ_1) CO08 data[25], which overlap with the present energy regime, are shown for comparison. The Geant4 simulated yield curve is depicted using the *R*-matrix fit ('Fit 1'). Here, E_p denotes the proton beam energy delivered from the accelerator. **b**, Three probable astrophysical *S*-factor curves (a measure of the cross-section of nuclear reactions) for the $^{19}F(p, \gamma_1)^{20}Ne$ reaction fitted by the *R*-matrix calculations. Six data points are derived from the present JUNA experiment. The uncertainties are purely statistical. The error bars are invisible where they are smaller than the size of the data point. See Extended Data Fig. 4 for fitting covariance matrix. MeV b, megaelectronvolt barns.

oldest known stars in the Universe, SMSS0313-6708, and, based on previously published stellar models[2], suggested that a CNO breakout during hydrogen burning is the source of calcium (Ca) production, reporting [Ca/H] = −7.2 (ref. [6]). Another work[15] also cited such a breakout as the Ca production mechanism for the stars HE 1327-2326 and HE 0107-5240, with [Ca/H] = −5.3 and −5.13, respectively. Pop III stars begin their lives with primordial Big Bang composition and contract until the central temperature is high enough (approximately 0.1 GK) to ignite the 3α process, creating a small abundance of carbon[16]—for example, $X_{^{12}C} \approx 10^{-9}$—to serve as a catalyst and initiate the CNO cycles. Previous stellar evolution simulations[1], using the Nuclear Astrophysics Compilation of Reaction Rates (NACRE) rate set[3] that supersedes the rates used by ref. [2], confirmed that the CNO cycling takes place at a core H-burning temperature of up to approximately 0.12 GK. Their nucleosynthesis calculations found that it was unlikely that large amounts of Ca could be produced by hot CNO breakout. Their predicted Ca abundance was between approximately 0.8 and nearly 2 dex lower than required by observations of the most metal-poor stars. If, however, the ratio of the $^{19}F(p, \gamma)^{20}Ne$ and the $^{19}F(p, \alpha)^{16}O$ reaction rates were a factor of approximately ten higher than that reported in the NACRE compilation[3], their models could produce Ca at the level observed in ultra-metal-poor stars such as SMSS0313-6708.

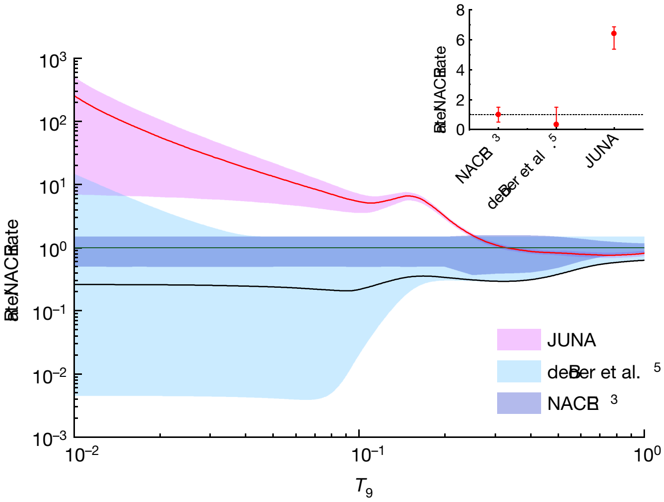

Fig. 2 | Ratio of the present (labelled as JUNA) relative to the NACRE rate[3]. The corresponding ratio for the rate of deBoer et al.[5] is also shown for comparison. The associated uncertainties are shown as the coloured bands. Inset, the ratios at a temperature of 0.14 GK. T_9 represents the temperature in 10^9 kelvin (that is, in gigakelvin, GK).

SMSS0313-6708 is an ultra-metal-poor star that is speculated to be a direct decedent of the first generation of stars in the Universe that formed after the Big Bang. The observable composition of an ultra-metal-poor star is a time capsule to the environment before the first galaxies formed—complementing the exciting upcoming observations of the James Webb Space Telescope[9], which is now aiming to give a first look at the earliest stars and galaxies.

Here the $(p, \gamma)/(p, \alpha)$ rate ratio is an invaluable tool with which to diagnose how the first stars evolved and died, and has far-reaching implications on stellar modelling. If Ca were produced from such hot hydrogen burning, the Ca produced in the later Si-burning phases can fall back onto a central black hole during the supernova[17], which is a key ingredient in the prevailing faint supernova with efficient fallback scenario. Otherwise, such a scenario has to be revised, or an alternative source must be validated. Other potential sources include a convective–reactive light pop III *i* process[18] or Ca synthesis from explosive burning[19]. Therefore, an accurate determination of the $^{19}F(p, \gamma)^{20}Ne$ rate around 0.1 GK is extremely important to pin down the origin of Ca made by pop III stars, as well as validating stellar evolution models.

In the centre-of-mass energy region of primary astrophysical interest (E_{COM} < 1 MeV), very limited experimental data are available for the $^{19}F(p, \gamma)^{20}Ne$ reaction, owing to the very strong 6.130-MeV γ-ray background from the competing $^{19}F(p, \alpha\gamma)^{16}O$ channel. This makes measurements of such small $^{19}F(p, \gamma)^{20}Ne$ cross-sections extremely difficult. Most of the previous experiments detected the greater than 11 MeV primary transition to the first excited state of ^{20}Ne (refs. [20–24]) using small-volume NaI(Tl) detectors with low resolution and efficiency. The earlier measurements also suffered from pileup from the 6.130-MeV γ-rays because of insufficient energy resolution to separate the two components. Later, a coincident detection technique[25] (between HPGe and NaI detectors) was developed to measure the $^{19}F(p, \gamma)^{20}Ne$ and $^{19}F(p, \alpha\gamma)^{16}O$ reactions over an energy range of E_{COM} = 200–760 keV. Owing to their limited sensitivity, only an upper limit for the strength of the E_{COM} = 213 keV resonance was given and no estimate was made for the 225-keV resonance, although it had been previously observed as a resonance in the $^{19}F(p, \alpha\gamma)^{16}O$ reaction[26]. Williams et al.[27] measured a factor of two larger strength value than that of ref. [25] for the 323-keV resonance by using the inverse kinematics method, because their measurement also included contribution owing to the ground-state transition. Recently, deBoer et al.[5] reanalysed the available $^{19}F(p, \gamma)^{20}Ne$

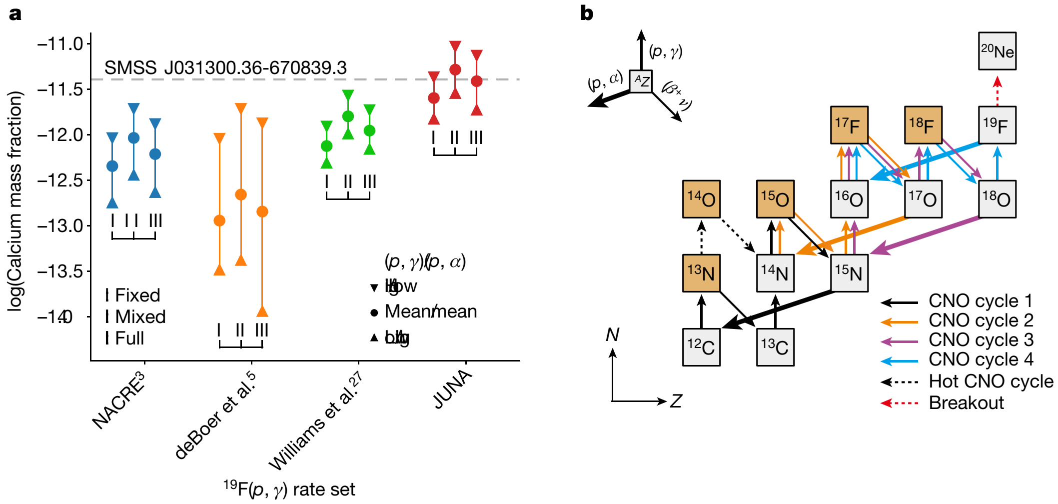

Fig. 3 | Prediction of calcium abundances with different rate set, and the CNO cycles. a, Range of results for different rate combinations and different modelling techniques[3,5,27]. (I) indicates trajectories of fixed temperature and density; (II) is for time-dependent trajectories (Supplementary Fig. 2) that include the effect of mixing due to convection; and (III) is for yields from full stellar models. **b**, The four classical CNO cycles[13] (solid lines) and the hot CNO cycle shortcut (black dotted lines). The breakout $^{19}F(p, \gamma)^{20}Ne$ reaction route is indicated by the red dotted arrow. See Supplementary Information for more details.

and $^{19}F(p, \alpha)^{16}O$ experimental data in the *R*-matrix framework, and estimated the corresponding rates for these two reactions. The pop III star Ca production problem, however, was intensified with their estimated ratio of the $^{19}F(p, \gamma)^{20}Ne$ and $^{19}F(p, \alpha)^{16}O$ rates, where the ratio was about a factor of four lower than that of NACRE.

So far, there is a scarcity of experimental data in the energy region below $E_{COM} \approx 0.35$ MeV. To provide an accurate thermonuclear rate, it is of paramount importance to directly measure the $^{19}F(p, \gamma)^{20}Ne$ reaction cross-section in this region. Because the cosmic-ray background radiation is very strong on the Earth's surface—that is, in aboveground laboratories—direct measurements of such small cross-sections are extremely challenging. The China JinPing Underground Laboratory (CJPL) is located in a traffic tunnel of a hydropower station under Jinping Mountain in the southwest of China[7], and has about 2,400 m of vertical rock overburden. By this measure, it is the deepest operational underground laboratory for particle and nuclear physics experiments in the world. It offers a great reduction in the muon and neutron fluxes by six and four orders of magnitude, respectively, compared to those at the Earth's surface. The cosmic-ray-induced background measured at CJPL[8] is about two orders of magnitude lower than that in the Laboratory for Underground Nuclear Astrophysics (LUNA; 1,400-m-thick dolomite rocks)[28]. With such a unique ultralow-background environment, the Jinping Underground Nuclear Astrophysics Experiment (JUNA)[29] was initiated, and we have performed a $^{19}F(p, \gamma)^{20}Ne$ direct measurement campaign as one of the day-one experiments.

The experiment was performed in normal kinematics using a high-current 400-kV electrostatic accelerator[30] at CJPL. A well focused, high-intensity proton beam uniformly impinged on a ^{19}F water-cooled target with a current up to approximately 1 mA. The experimental set-up is shown in Extended Data Fig. 1. Durable implanted ^{19}F targets[31] were used in both $^{19}F(p, \alpha\gamma)^{16}O$ (ref. [32]) and $^{19}F(p, \gamma)^{20}Ne$ experiments. The γ-rays were detected using a nearly 4π bismuth germanate (BGO) detector array that was also used in the preceding JUNA experiments[32,33]. Typical γ-ray spectra are shown in Extended Data Fig. 2. Owing to the different detection efficiency, the contribution of the summing γ_{sum}-rays (at approximately 13 MeV) from the $^{19}F(p, \gamma)^{20}Ne$ reaction has been separated into two components: one involves only the transition to the ground state in ^{20}Ne, hereafter referred to as (p, γ_0); another involves all transitions through the 1.634 MeV first excited state to the ground state in ^{20}Ne, hereafter referred to as (p, γ_1). In this way, the (p, γ_1) component can be precisely determined based on the coincident technique described here, because the nearby heavy summing signal (at approximately 12 MeV) induced by the 6.130-MeV γ-rays interferes with the total counts of the summed γ-rays, as do those γ-rays from the $^{11}B(p, \gamma)^{12}C$ contamination reaction at lower proton energies. As shown in the inset of Extended Data Fig. 2, the 1.634 → ground state transition can be clearly observed by gating on the summing γ_{sum}-rays, which correspond to the $^{19}F(p, \gamma_1)^{20}Ne$ component. Figure 1a shows the resulting 1.634 MeV γ-ray yields obtained using this coincidence technique.

We find a resonance at $E_{COM} = 225$ keV, well below the well known resonance at $E_{COM} = 323$ keV. For the known 323-keV resonance, the γ-yield ratios between the $(p, \alpha\gamma)$ and (p, γ) channels obtained are shown in Extended Data Fig. 3. We determined partial strengths of $\omega\gamma_{(p,\gamma_1)} = 2.09 \pm 0.21$ meV and $\omega\gamma_{(p,\gamma_0)} = 1.07 \pm 0.21$ meV, respectively. Thus, its total strength is determined to be $\omega\gamma_{(p,\gamma_{tot})} = 3.16 \pm 0.33$ meV, where the statistical and systematic errors are 0.23 meV and 0.24 meV, respectively. The present $\omega\gamma_{(p,\gamma_1)}$ value is about a factor of 1.5 larger than the previous value of 1.38 ± 0.44 meV (ref. [25]). Both values agree within a 2σ uncertainty, but our value has much improved precision. In addition, our total value of $\omega\gamma_{(p,\gamma_{tot})}$ is consistent with the NACRE adopted value of 5 ± 3 meV, as well as with the recently reported value of $3.3^{+1.1}_{-0.9}$ meV (ref. [27]) that was also sensitive to the direct capture to ground state, but with 4–7 times better precision. For the observed 225-keV resonance, its strength is determined to be $\omega\gamma_{(p,\gamma_1)} = (4.19 \pm 0.33) \times 10^{-2}$ meV based on the yield ratio between the 323-keV $(p, \alpha\gamma)$ and 225-keV (p, γ_1) resonances. Our resonance strengths were all determined relative to the well known $(p, \alpha\gamma)$ strength of the $E_{COM} = 323$ keV resonance. Here the yield corresponds to the integrated γ-ray counts (corrected for efficiency) under the yield curve over the resonance. We find that the (p, γ_0) contribution is negligibly small in the energy region below $E_{COM} \approx 322$ keV (see Fig. 1a), and hence $\omega\gamma_{(p,\gamma_{tot})} \approx \omega\gamma_{(p,\gamma_1)}$ for this resonance. For the previously theorized $E_{COM} = 213$ keV resonance, estimates placed upper limits on the strength at 1.3×10^{-3} meV (ref. [3]) and 9.3×10^{-4} meV (ref. [25]); we now firmly constrain its strength to be less than 4.2×10^{-3} meV (that is, less than 10% of that of the 225-keV resonance), on the basis of the present experimental data. Table 1 summarizes the resonance properties.

A multilevel, multichannel *R*-matrix analysis, using the code AZURE2[34,35], was used to fit the data. The *R*-matrix analysis is an extension of that presented in ref. [5], and includes all those data, together

Table 1 | Relevant resonance strengths $\omega\gamma_{tot}$

E_{COM} (keV)	E_x (MeV)	J^π	$\omega\gamma_{tot}$ (meV)		ANC ($fm^{-1/2}$)	Γ_{α_2} (eV)	Γ_{γ_1} (eV)
			Present	NACRE[3]			
−448	12.396(4)[a]	1^+			15[b]	60^{+40}_{-30}	<3.4
11	12.855(4)[a]	1^+			1.14×10^{-28}[c]	-590^{+230}_{-290}	<4.8
212.7(10)	13.057	2^-	$<4.2\times10^{-3}$	$<1.3(13)\times10^{-3}$			
225.2(10)	13.069	3^-	$4.19(33)\times10^{-2}$				
323.9	13.168(2)[b]	1^+	3.16(33)	5(3)			

Values are determined for the $^{19}F(p,\gamma)^{20}Ne$ reaction (with total errors listed in parentheses). *R*-matrix fit parameters are tabulated, including sub-threshold and near-threshold 11-keV resonances as shown in Fig. 1b. The fit includes the additional levels and from ref.[5] as fixed background terms. See Methods for details.

E_x values fixed to those determined in previous analyses are indicated by: [a]ref.[39], [b]ref.[5], [c]ref.[26], where the corresponding uncertainties are adopted. $\Gamma_{\alpha2}$, partial width of $\alpha2$-decay channel; $\Gamma_{\gamma1}$, partial width of $\gamma1$-decay channel; ANC, asymptomatic normalization coefficient; J^π, spin-parity.

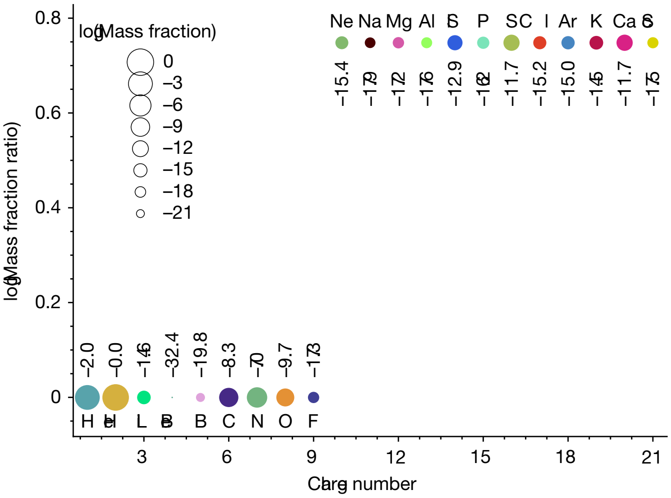

Fig. 4 | Ratio of final abundances of using our JUNA mean $^{19}F(p,\gamma)$ rate compared to using the NACRE[3] mean rate. Both use the NACRE mean $^{19}F(p,\alpha)$ rate. The ratio is shown at core hydrogen depletion, at a hydrogen mass fraction of 0.01 and using the mixing model. The linear size of the symbol indicates the logarithm of the absolute mass fraction (see legend). Their numerical values are given adjacent to the symbols.

with the new CJPL (p,γ_1) and $(p,\alpha\gamma)$ data. With this method, various possible contributions can be strictly constrained. The curve shown in Fig. 1a represents the Geant4[36] simulated results by using one of the lowest χ^2 *R*-matrix fits ('Fit 1') to the *S*-factor data. Figure 1b shows six off-resonance data points derived from the present JUNA experiment. Numeric samples of the *S* factors and the associated uncertainties in the off-resonance region are tabulated in Extended Data Table 1. We present the three best *R*-matrix fits. Here 'sub' denotes the 1^+ sub-threshold state at $E_x = 12.396$ MeV, and '11 keV' denotes the 11 keV 1^+ resonance at $E_x = 12.855$ MeV. For example, the label 'Fit 1: sub, 11 keV' indicates the *R*-matrix fit including both the sub-threshold state and the 11-keV resonance. The nuclear level properties in the *R*-matrix fits were co-varied over a large parameter space. The resultant resonance properties deduced from the *R*-matrix fits are listed in Table 1 (see Methods for details of the *R*-matrix calculations).

The thermonuclear $^{19}F(p,\gamma)^{20}Ne$ reaction rate as a function of temperature is calculated by numerical integration of the *S* factors shown in Fig. 1b[11]. The mean rate and the associated uncertainties (low and high limits) are obtained in a temperature region of 0.01–1 GK and presented in Extended Data Table 2. The ratios between the present rate and the NACRE recommended rate are shown in Fig. 2. It shows that our rate is enhanced by a factor of 5.4–7.4 at the temperature around 0.1 GK. This enhancement is attributed to the observed 225-keV resonance. In addition, our rate is about 200 times larger at temperatures around 0.01 GK, primarily owing to the 11-keV resonance[32]. The uncertainty of the present rate is drawn as a coloured band, which we estimate based on the uncertainties of the resonance strengths and *R*-matrix calculations. The uncertainties in the present *S* factor and rate over the range of astrophysical interest have been greatly reduced compared to previous estimates[5].

deBoer et al.[5] recommended a $^{19}F(p,\alpha)^{16}O$ mean rate similar to that of NACRE[3]. Thus, we adopt the NACRE $^{19}F(p,\alpha)^{16}O$ rate as our reference, and hence obtain an enhancement factor of 5.4–7.4 for the $(p,\gamma)/(p,\alpha)$ rate ratio relative to that of NACRE[3] at around 0.1 GK. We find an even larger enhancement below approximately 0.08 GK. By a simple scaling argument to the model calculations in refs. [1,5], the observed Ca abundances in the oldest known SMSS0313-6708 star can now be reproduced reasonably with our $^{19}F(p,\gamma)^{20}Ne$ rate.

We have investigated the effect of the thermonuclear $^{19}F(p,\gamma)^{20}Ne$ rate on a range of nucleosynthesis modelling techniques, and the calcium production is summarized in Fig. 3a. Our studies comprise simple trajectories (see Extended Data Table 3), new mix models (see Extended Data Table 4), and full stellar models (see Extended Data Table 5) calculations. We find that all our nucleosynthesis models can reproduce the observed calcium production. We conclude that the ^{40}Ca observed in the oldest known ultra-iron-poor stars (for example, SMSS0313-6708) may indeed originate in hydrostatic burning in pop III stars, requiring only the supernova ejection of their outer layers, whereas the metal-rich core may collapse to a black hole. Previously, the ejection of the metal-rich core was required as the source of calcium abundance observed in the oldest stars. On the contrary, here we show a much stronger breakout from a 'warm' CNO cycle scenario via $^{19}F(p,\gamma)^{20}Ne$ (Fig. 3b), which substantially increases the production of Ne–Ca. Figure 4 shows the ratio of final abundances of using our JUNA mean $^{19}F(p,\gamma)$ rate compared to using the NACRE mean rate. The production of all elements beyond $Z = 9$ is shifted by a constant factor and hence can be well represented by single species, for example, the double-magic nucleus ^{40}Ca that was observed in ultra-metal-poor stars. This clearly shows the bottleneck nature of the $^{19}F(p,\gamma)$–$^{19}F(p,\alpha)$ branching point. See Supplementary Information for more details.

To conclude, we have directly measured the $^{19}F(p,\gamma)^{20}Ne$ reaction down to the very low energy point of $E_{COM} \approx 186$ keV by exploiting the extremely low-background environment deep underground, the high-intensity beam and newly developed durable target(s). These unique and featured conditions enabled us to measure this crucial reaction at the stellar energy region, which has been previously inaccessible in aboveground laboratories. We report on a key resonance at 225 keV and determine a precise thermonuclear rate over the temperature region of astrophysical importance. Our enhanced rate leads to a stronger breakout in a 'warm' CNO scenario as the origin of the calcium discovered in the oldest, ultra-iron-poor stars. Our results provide a strong experimental foundation for the faint supernova model of first-generation primordial stars as a source for the observed chemical abundance signature. The astrophysical implications of our reported rate on novae, X-ray bursts, AGB (asymptotic giant branch) stars and other star sites are still subject to future detailed investigation.

Online content

Any methods, additional references, Nature Research reporting summaries, source data, extended data, supplementary information, acknowledgements, peer review information; details of author contributions and competing interests; and statements of data and code availability are available at https://doi.org/10.1038/s41586-022-05230-x.

1. Clarkson, O. & Herwig, F. Convective H–He interactions in massive population III stellar evolution models. *Mon. Not. R. Astron. Soc.* **500**, 2685–2703 (2021).
2. Heger, A. & Woosley, S. E. Nucleosynthesis and evolution of massive metal-free stars. *Astrophys. J.* **724**, 341–373 (2010).
3. Angulo, C. et al. A compilation of charged-particle induced thermonuclear reaction rates. *Nucl. Phys. A* **656**, 3–183 (1999).
4. Arnould, M., Mowlavi, N. & Champagne, A. E. In *Stellar Evolution: What Should Be Done?, Proc. 32nd Liège International Astrophysical Colloquium* (eds Noels, A. et al) 17–29 (Université de Liège, 1995).
5. deBoer, R. J. et al. ^{19}F(p, γ)^{20}Ne and ^{19}F(p, α)^{16}O reaction rates and their effect on calcium production in Population III stars from hot CNO breakout. *Phys. Rev. C* **103**, 055815 (2021).
6. Keller, S. C. et al. A single low-energy, iron-poor supernova as the source of metals in the star SMSS J031300.36−670839.3. *Nature* **506**, 463–466 (2014).
7. Kang, K. J. et al. Status and prospects of a deep underground laboratory in China. *J. of Phys. Conf. Ser.* **203**, 012028 (2010).
8. Wu, Y. C. et al. Measurement of cosmic ray flux in the China JinPing underground laboratory. *Chin. Phys. C* **37**, 086001 (2013).
9. Witze, A. The James Webb Space Telescope aims to unlock the early Universe. *Nature* **600**, 208–212 (2021).
10. Burbidge, E. M., Burbidge, G. R., Fowler, W. A. & Hoyle, F. Synthesis of the elements in stars. *Rev. Mod. Phys.* **29**, 547–654 (1957).
11. Rolfs, C. E. & Rodney, W. S. *Cauldrons in the Cosmos* (Univ. Chicago Press, 1988).
12. Adelberger, E. G. et al. Solar fusion cross sections. II. The *pp* chain and CNO cycles. *Rev. Mod. Phys.* **83**, 195–245 (2011).
13. Wiescher, M., Görres, J. & Schatz, H. Break-out reactions from the CNO cycles. *J. Phys. G* **25**, R133–R161 (1999).
14. Frebel, A. & Norris, J. E. Near-field cosmology with extremely metal-poor stars. *Ann. Rev. Astron. Astrophys.* **53**, 631–688 (2015).
15. Takahashi, K., Umeda, H. & Yoshida, T. Stellar yields of rotating first stars. I. Yields of weak supernovae and abundances of carbon-enhanced hyper-metal-poor stars. *Astrophys. J.* **794**, 40 (2014).
16. Ezer, D. & Cameron, A. G. W. The evolution of hydrogen–helium stars. *Astrophys. Space Sci.* **14**, 399–421 (1971).
17. Chan, C., Müller, B. & Heger, A. Black hole formation and fallback during the supernova explosion of a 40$M_{\odot}$ star. *Astrophys. J.* **852**, L19 (2018).
18. Clarkson, O., Herwig, F. & Pignatari, M. Pop III *i*-process nucleosynthesis and the elemental abundances of SMSS J0313-6708 and the most iron-poor stars. *Mon. Not. R. Astron. Soc.* **474**, L37–L41 (2018).
19. Limongi, M. & Chieffi, A. Presupernova evolution and explosive nucleosynthesis of zero metal massive stars. *Astrophys. J. Supp. Ser.* **199**, 38 (2012).
20. Sinclair, R. M. Gamma radiation from certain nuclear reactions. *Phys. Rev.* **93**, 1082–1086 (1954).
21. Farney, G. K., Given, H. H., Kern, B. D. & Hahn, T. M. High-energy gamma rays from the proton bombardment of fluorine. *Phys. Rev.* **97**, 720–725 (1955).
22. Keszthelyi, L., Berkes, I., Demeter, I. & Fodor, I. Resonances in F^{19}+p reactions at 224 and 340 keV proton energies. *Nucl. Phys.* **29**, 241–251 (1962).
23. Berkes, I., Dézsi, I., Fodor, I. & Keszthelyi, L. The resonance at 483 and 597 keV proton energies in F^{19}+p reactions. *Nucl. Phys.* **43**, 103–109 (1963).
24. Subotíc, K. M., Ostojíc, R. & Stepančić, B. Z. Study of the ^{19}F(p, γ)^{20}Ne radiative capture reaction from 0.2–1.2 MeV. *Nucl. Phys. A* **331**, 491–501 (1979).
25. Couture, A. et al. Measurement of the ^{19}F(p, γ)^{20}Ne reaction and interference terms from $E_{\mathrm{c.m.}}$ = 200–760 keV. *Phys. Rev. C* **77**, 015802 (2008).
26. Spyrou, K. et al. Cross section and resonance strength measurements of ^{19}F(p,$\alpha\gamma$)^{16}O at E$_p$=200–800 keV. *Eur. Phys. J. A* **7**, 79–85 (2000).
27. Williams, M. et al. New measurement of the $E_{\mathrm{c.m.}}$ = 323 keV resonance in the ^{19}F(p, γ)^{20}Ne reaction. *Phys. Rev. C* **103**, 055805 (2021).
28. Broggini, C., Bemmerer, D., Guglielmetti, A. & Menegazzo, R. LUNA: nuclear astrophysics deep underground. *Ann. Rev. Nucl. Part. Sci.* **60**, 53–73 (2010).
29. Liu, W. P. et al. Progress of Jinping Underground laboratory for Nuclear Astrophysics (JUNA). *Sci. China Phys. Mech. Astron.* **59**, 642001 (2016).
30. Wu, Q. et al. Design of an intense ion source and LEBT for Jinping Underground Nuclear Astrophysics experiments. *Nucl. Instr. Meth. A* **830**, 214–218 (2016).
31. Zhang, L. Y. et al. Strong and durable fluorine-implanted targets developed for deep underground nuclear astrophysical experiments. *Nucl. Instr. Meth. B* **496**, 9–15 (2021).
32. Zhang, L. Y. et al. Direct measurement of the astrophysical ^{19}F(p,$\alpha\gamma$)^{16}O reaction in the deepest operational underground laboratory. *Phys. Rev. Lett.* **127**, 152702 (2021).
33. Su, J. et al. First result from the Jinping Underground Nuclear Astrophysics experiment JUNA: precise measurement of the 92-keV ^{25}Mg(p, γ)^{26}Al resonance. *Sci. Bull.* **67**, 125–132 (2022).
34. Azuma, R. E. et al. AZURE: An *R*-matrix code for nuclear astrophysics. *Phys. Rev. C* **81**, 045805 (2010).
35. Uberseder, E. & deBoer, R. J. *AZURE2 User Manual* (2015).
36. Agostinelli, S. et al. Geant4—a simulation toolkit. *Nucl. Instrum. Meth. A* **506**, 250–303 (2003).

Methods

JUNA experiment

The Jinping Underground Nuclear Astrophysics Experiment (JUNA)[29] was initiated in 2015. One of the day-one goals[37] was to directly measure the $^{19}F(p, \alpha\gamma)^{16}O$ reaction at Gamow energies. The measurement was accomplished and results were published elsewhere[32]. The present $^{19}F(p, \gamma)^{20}Ne$ experiment was immediately followed that $(p, \alpha\gamma)$ run with the same experiment set-up, acting as one of the day-one campaigns. The combination of the ultralow-background environment, the strong beam intensity, the durable target and the coincidence technique ultimately makes this direct $^{19}F(p, \gamma)^{20}Ne$ measurement possible.

The schematic view of the experimental set-up is shown in Extended Data Fig. 1. A proton beam from the accelerator was undulated over a rectangular area of about 4 × 4 cm^2 by oscillating the magnetic field of the beam deflector. A well focused, intense beam was uniformly spread across the target, mitigating damage to the target. The scanning proton beam was collimated by two apertures (ϕ15 upstream and ϕ12 mm downstream, where ϕ indicates diameter) and then impinged on a water-cooled target, where the beam current reached up to 1 mA, with a spot size of about ϕ10 mm. An inline Cu shroud cooled to LN_2 temperature extended close to the target to minimize carbon build-up on the target surface. Together with the target, the Cu shroud constituted the Faraday cup for beam integration. A negative voltage of 300 V was applied to the shroud to suppress secondary electrons from the target. A very strong and durable implanted ^{19}F target[31] was used in this work. The optimum scheme for target production is: first, implanting ^{19}F ions into the pure Fe backings with an implantation energy of 40 keV, and then sputtering a 50-nm-thick Cr layer to further prevent the fluorine material loss. The 4π $Bi_4Ge_3O_{12}$ (BGO) detector array specially designed for the JUNA project is composed of eight identical segments with a length of 250 mm and a radial thickness of 63 mm, each covering a 45° azimuthal angle. For the 6.130-MeV γ-rays, the total absolute detection efficiency was ~58%, with a ~6% energy resolution achieved by alcohol-cooling the BGO crystals (~−5 °C). To further suppress the natural background emitted from the rocks and induced by neutron capture reactions, the BGO array was passively shielded by 5-mm copper, 100-mm lead and 1-mm cadmium, respectively. By adjusting the beam intensity in each run, the counting rate of the BGO array was limited to about 10 kHz to prevent the signal pileups and reduce the dead-time of the data acquisition (DAQ) system. In addition, the waveforms of pulses were recorded in the DAQ system to monitor the pileup events during the experiment. We found that the pileup events are very rare, and can be completely ignored.

Extended Data Fig. 2 shows the typical γ-ray spectra taken for two typical energy points, $E_p = 356$ keV (a) and at $E_p = 250$ keV (b). Here E_p denotes the proton beam energy delivered from the accelerator, and the real bombarding energy on the fluorine atoms is reconstructed by taking into account the energy loss through the Cr protective layer with a Geant4 simulation[36]. It shows that the 6.130-MeV γ-rays (from the $\alpha\gamma_2$ channel) dominate the whole spectra, whereas the 6.917-MeV (from the $\alpha\gamma_3$ channel) and 7.117-MeV (from the $\alpha\gamma_4$ channel) γ-rays observed at certain proton energies only make a maximum contribution of ~2.4% in the energy region studied in this work. Here we are mainly concerned with the summing γ-ray peak for the targeted $^{19}F(p, \gamma)^{20}Ne$ channel around 13 MeV. The γ-rays induced by the ^{11}B, ^{12}C and ^{13}C contaminants were observed at certain energies, and their origins were clearly identified[31,32]. The ^{19}F target material loss was monitored and found to be negligible since the total beam dose utilized in this measurement was only about 41 C, which was consistent with prior expectations[31].

A precise determination of the absolute ^{19}F number density is challenging because of the complicated target structure and the unknown self-sputtering rate during the implantation procedure. Similar to previous work[32], we derived the (p, γ) strengths of the 225-keV and 323-keV resonances relative to the well known $(p, \alpha\gamma)$ strength of the 323-keV resonance. Its strength was evaluated as $\omega\gamma_{(p,\alpha\gamma)} = 23.1 \pm 0.9$ eV in NACRE—that is, with an uncertainty of about 4%. For the 323-keV resonance, the ratios between $(p, \alpha\gamma)$ and (p, γ) yields are obtained at five energy points over the resonance, by comparing the corresponding γ-ray counts corrected by the efficiency. The corresponding ratios are shown in Extended Data Fig. 3. The weighted average ratios and the associated uncertainties are plotted as the solid and dashed lines, respectively. We find weighted average ratios of $(p, \alpha\gamma)/(p, \gamma_1)$ and $(p, \alpha\gamma)/(p, \gamma_0)$ of $(1.11 \pm 0.07) \times 10^4$ and $(2.15 \pm 0.39) \times 10^4$, respectively.

Astrophysical *S* factors

Selected astrophysical *S* factors derived for the $^{19}F(p, \gamma)^{20}Ne$ reaction in the non-resonance region are listed in Extended Data Table 1, which are shown in Fig. 1b (with statistical uncertainties shown only). Here the statistical uncertainties range from 8.3% to 27.4%, as listed in the last column of Extended Data Table 1. The systematic uncertainties mainly include the following contributions: (1) a 5% uncertainty estimated for the Geant4 simulation by assuming a 0.5-keV uncertainty in the reconstructed E_{COM} energy; (2) a 3.9% uncertainty of the 323-keV resonance strength (from the normalization); and (3) a 5%–10% uncertainty of the 1,634-keV γ-ray coincidence efficiency. From this, conservatively, we estimate an overall systematic uncertainty of 12%.

R-matrix fit

The temperature relevant to the population III stars is about 0.1–0.12 GK, corresponding to an energy range around 100 keV. At such low energies, the Coulomb repulsion between the two interacting particles—proton and ^{19}F—makes the cross-sections so small that their laboratory measurement is very challenging owing to the low event rate. Therefore, measurements are typically made at higher energies, and then a model with underlying physical motivation is used to extrapolate to the low energies of interest. In low-energy nuclear physics, *R*-matrix analysis is one of the most successful of these phenomenological reaction models. The model is both very flexible, applicable to various reactions, yet still has fundamental physical constraints.

At JUNA, we have obtained both $^{19}F(p, \gamma)^{20}Ne$ and $^{19}F(p, \alpha\gamma)^{16}O$ cross-section data. The latter was already described elsewhere[32]. Although the $^{19}F(p, \gamma)^{20}Ne$ cross-section measurements extend to lower energies than previous measurements, they are still higher in energy than the energy range of interest to astrophysics. Therefore the AZURE2[34,35] *R*-matrix code has been used to simultaneously fit both reactions using our data. This *R*-matrix analysis is an extension of earlier work presented in ref. [5].

It remains unknown which resonance contributions dominate at very low energies, and therefore several *R*-matrix fits were attempted, taking into account different contributions from either a sub-threshold resonance ('sub') or a near-threshold resonance at 11 keV ('11 keV'). The three most probable fit solutions are shown in Fig. 1b. To quantify the uncertainty stemming from the experimental data and the ambiguity in the low-energy resonance structure, a Bayesian uncertainty analysis has been performed[38]. Extended Data Fig. 4 shows the covariance matrix from a Markov chain Monte Carlo (MCMC) analysis that includes Γ_{γ_1} for both the sub-threshold and near-threshold resonances. The data indicate that at least one of these components is needed. When both are included, the MCMC analysis indicates a non-zero contribution from the sub-threshold resonance contribution and a value that is consistent with zero for the near-threshold resonance. This analysis quantifies an upper limit for the *S*-factor extrapolation as indicated in Fig. 1b at the 68% level. A lower limit is calculated using an analysis that only includes the sub-threshold resonance, resulting in a nearly constant low-energy *S*-factor. In Table 1, E_x values that are fixed to those determined in previous analyses are indicated by the footnotes a[39], b[5] and c[26], where the corresponding uncertainties are adopted, whereas for the present results, an assumed uncertainty of 1.0 keV is quoted on the resonance energies. The sign of a partial width indicates the sign of the corresponding reduced-width amplitude. No uncertainties are quoted for the ANCs of both the bound and near-threshold states as none are available from previous literature. Further, the present data constrain only the product of the ANC and the γ width and we have chosen to indicate this uncertainty on the γ width. The details will be published elsewhere.

Reaction rates

At each temperature point in Fig. 2, three reaction rates were calculated based on the three S-factor curves shown in Fig. 1b. The maximum and minimum of the three rates were adopted as the high and low limits, and the average of the maximum and minimum was adopted as the recommended median rate. Where the rate errors (that is, low and high limits) are smaller than those caused by the JUNA S-factor errors, the S-factor errors were adopted accordingly as the total reaction rate error (that is, low and high limits). In this way, the present median rate and the associated uncertainties are obtained in a temperature region of 0.01–1 GK. Beyond 1 GK, the NACRE rates can be used. Extended Data Table 2 lists the presently recommended thermonuclear $^{19}\mathrm{F}(p,\gamma)^{20}\mathrm{Ne}$ rates, and the associated uncertainties (low and high values).

The present mean rate can be parameterized by the standard format of ref. [40],

$$
\begin{aligned}
N_A\langle\sigma v\rangle = \exp\Big(&-8.41786 - \frac{3.8921}{T_9} + \frac{30.2621}{T_9^{1/3}} - 66.1213T_9^{1/3} \\
&+128.424T_9 - 94.5477T_9^{5/3} + 8.01847\ln T_9\Big) \\
&+\exp\Big(6.20324 - \frac{2.65022}{T_9} - \frac{5.03462}{T_9^{1/3}} + 6.9107T_9^{1/3} \\
&-0.999798T_9 + 0.0523095T_9^{5/3} - 0.733785\ln T_9\Big) \\
&+\exp\Big(27.5327 - \frac{10.7563}{T_9} - \frac{11.5633}{T_9^{1/3}} - 6.36271T_9^{1/3} \\
&+6.62094T_9 - 1.306661T_9^{5/3} - 9.70975\ln T_9\Big) \\
&+\exp\Big(17.4989 + \frac{0.0127512}{T_9} - \frac{17.7464}{T_9^{1/3}} - 0.540527T_9^{1/3} \\
&+2.50115T_9 - 0.623077T_9^{5/3} - 1.33705\ln T_9\Big)
\end{aligned}
$$

with a fitting error of less than 1% over the temperature region of 0.01–1 GK.

Astrophysical calculations

We have investigated the effect of the thermonuclear $^{19}\mathrm{F}(p,\gamma)^{20}\mathrm{Ne}$ rate on a range of nucleosynthesis modelling techniques. We have performed a range of full stellar model calculations for a 40 $M_\odot$ star of initially primordial composition with the KEPLER code[41]. The calcium production is briefly summarized in Fig. 3a, and the numerical values are listed in Extended Data Tables 3–5 for simple trajectories, new mix models, and for full stellar model calculations, respectively. See Supplementary Information for more details.

Data availability

Experimental data taken at JUNA are proprietary to the collaboration but can be made available from the corresponding authors upon reasonable request.

Code availability

The R-matrix code can be made available upon request to R.J.dB. (richard.james.deboer@gmail.com).

37. He, J. J. et al. A proposed direct measurement of cross section at Gamow window for key reaction $^{19}\mathrm{F}(p,\alpha)^{16}\mathrm{O}$ in asymptotic giant branch stars with a planned accelerator in CJPL. *Sci. China Phys. Mech. Astron.* **59**, 652001 (2016).
38. Foreman-Mackey, D. et al. The MCMC hammer. *Publ. Astron. Soc. Pacif.* **125**, 306–312 (2013).
39. Kious, M. *Determination of nuclear reaction rates leading to the stellar nucleosynthesis of fluorine.* PhD thesis, Université de Paris-Sud (1990).
40. Rauscher, T. & Thielemann, F.-K. Astrophysical reaction rates from statistical model calculations. *At. Data Nucl. Data Tables* **75**, 1–351 (2000).
41. Weaver, T. A., Zimmerman, G. B. & Woosley, S. E. Presupernova evolution of massive stars. *Astrophys. J.* **225**, 1021–1029 (1978).
42. Pitrou, C., Coc, A., Uzan, J.-P. & Vangioni, E. Precision big bang nucleosynthesis with the new code PRIMAT. *JPS Conf. Proc.* **31**, 011034 (2020).

Acknowledgements We thank the staff of the CJPL and Yalong River Hydropower Development Company (N. C. Qi, W. L. Sun, X. Y. Guo, P. Zhang, Y. H. Chen, Y. Zhou, J. F. Zhou, J. R. He, C. S. Shang, M. C. Li) for logistics support. We thank F. Herwig, Y. Sun and S. E. Malek for discussions. We acknowledge support from the National Natural Science Foundation of China (nos. 11825504, 11490560, 12075027, 12125509). R.J.dB. and M.W. were supported by the NSF through grant no. Phys-2011890. R.J.dB., M.W. and A.H. were supported by the Joint Institute for Nuclear Astrophysics through grant no. PHY-1430152 (JINA Center for the Evolution of the Elements). A.H. was supported by the Australian Research Council (ARC) Centre of Excellence (CoE) for Gravitational Wave Discovery (OzGrav) through project number CE170100004, by the ARC CoE for All Sky Astrophysics in 3 Dimensions (ASTRO 3D) through project number CE170100013. D.K. acknowledges the support of the Romanian Ministry of Research and Innovation under research contract 10N/PN 19 06 01 05. D.O. was supported by the NSF through grant no. OAC-2004601.

Author contributions M.W. proposed the original idea of this research. J.H. and W.L. proposed this JUNA experiment. Liyong Zhang and J.H. designed the experimental set-up and led all the tests and experiments, and performed the data reduction and analysis. R.J.dB. and M.W. performed the R-matrix analysis. A.H. made the astrophysical model calculation and interpretation. J.S., Y.C., X.L., H. Zhang, X.J., L.W., Ziming Li and L. Song participated in the experiment. J.H., A.H., D.K., R.J.dB., M.W. and W.L. prepared the draft of the manuscript. D.K. made major contributions to the manuscript polishing. All authors read the manuscript, gave comments, suggested changes, and agreed with the final version. Long Zhang, F.C., Y.C. and Z.Z. took main responsibility for the operation of the JUNA accelerator. J.S. and Zhigong Li developed the 4π BGO detector array, and J.W. developed the DAQ system. L. Sun, Q.W., J.L. and H. Zhao designed and constructed the ECR ion source. B.C., L.C., R.M. and G.L. designed and constructed the 400-kV accelerator. J.H. supervised the experiment and verified that the data were acquired correctly as a PI of this subproject. W.L. leads the JUNA project, and J.C. leads the CJPL.

Competing interests The authors declare no competing interests.

Additional information
Supplementary information The online version contains supplementary material available at https://doi.org/10.1038/s41586-022-05230-x.
Correspondence and requests for materials should be addressed to Jianjun He, Michael Wiescher or Weiping Liu.
Peer review information *Nature* thanks Friedrich-Karl Thielemann and the other, anonymous, reviewer(s) for their contribution to the peer review of this work.
Reprints and permissions information is available at http://www.nature.com/reprints.

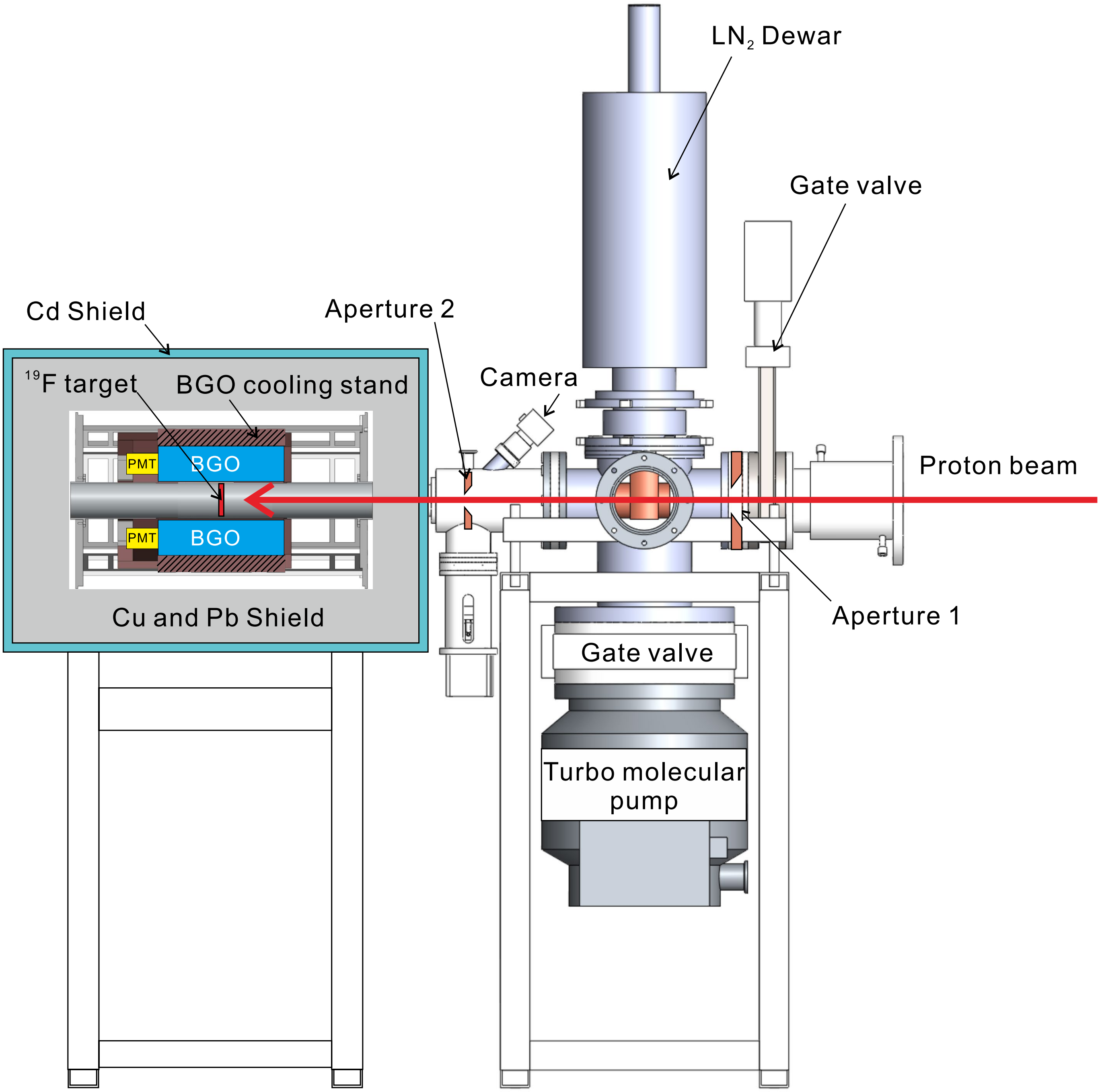

Extended Data Fig. 1 | The schematic view of the experimental set-up. The proton beam bombarded on the implanted ^{19}F target through two apertures. The beam spot on the last aperture was monitored by a camera. A LN$_2$-cooled trap extended close to the target to reduce the carbon build-up. The γ-rays were detected by a 4π BGO array with massive shielding.

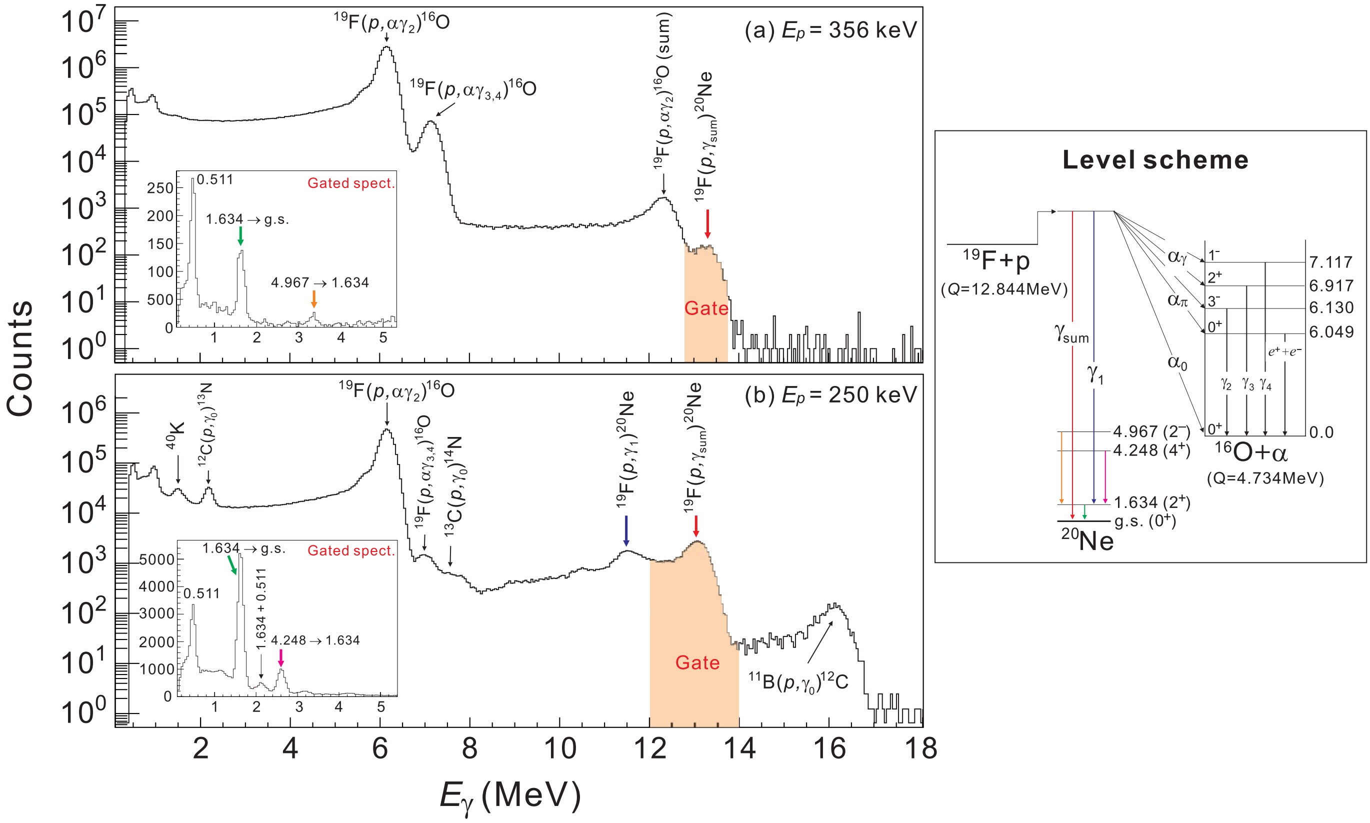

Extended Data Fig. 2 | Typical γ-ray spectra and corresponding level scheme. Left, Typical γ-ray spectra taken with a 4π BGO array at JUNA during proton bombardment of an implanted ^{19}F target, at proton energies of (a) 356 keV and (b) 250 keV. The heavy γ-ray background from the competing ^{19}F(p, $\alpha\gamma$)^{16}O channel and their summing signals are indicated. The summing γ-ray peak for the target ^{19}F(p, γ)^{20}Ne channel is indicated by red arrows. The inset shows the coincident γ-ray spectrum gated on the summing peak located in the shaded region. Right, The corresponding level scheme, where the summing γ-ray and the gated γ-ray transitions are illustrated by the coloured arrows.

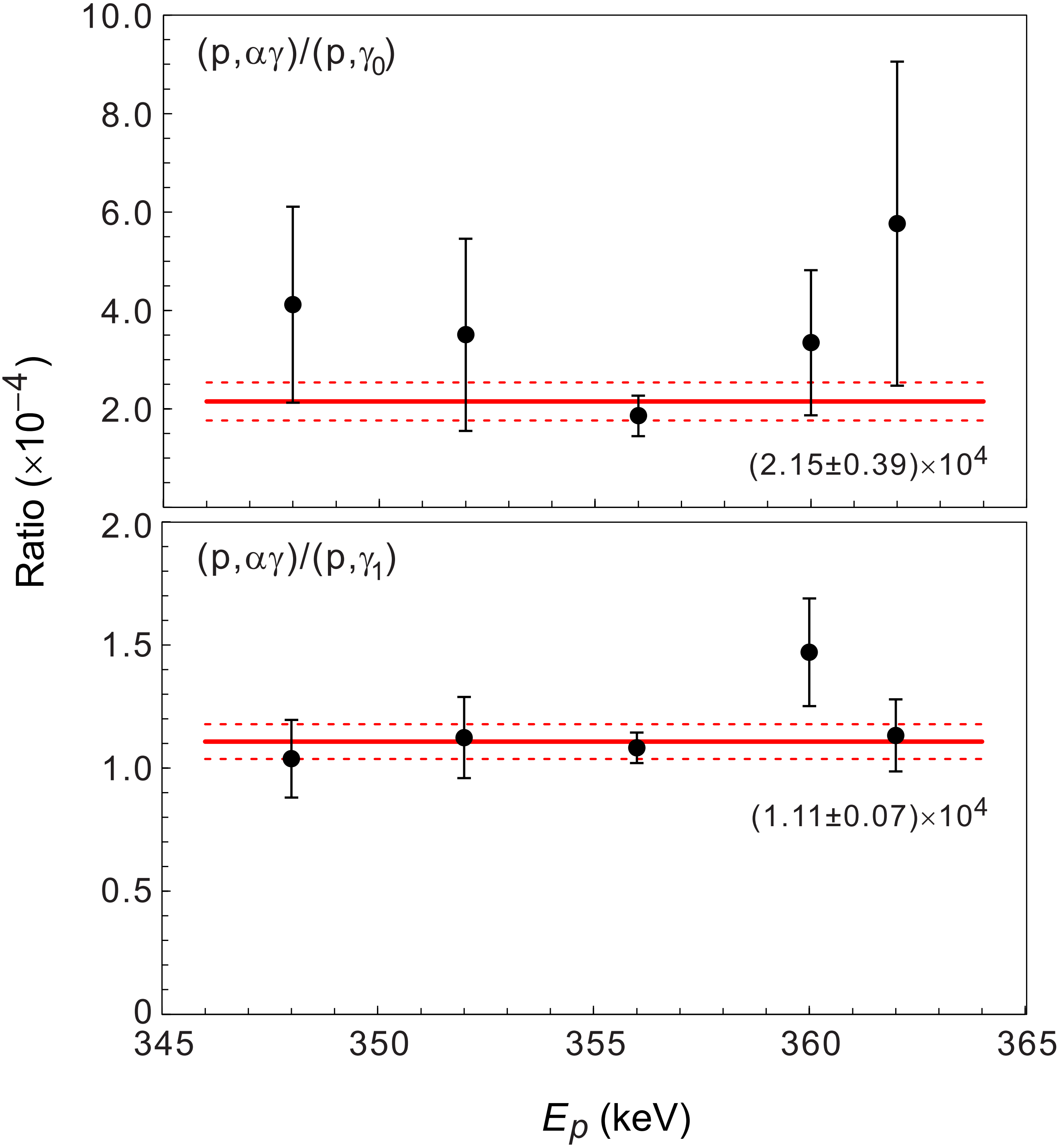

Extended Data Fig. 3 | Yield ratios of $(p, \alpha\gamma)/(p, \gamma_1)$ and $(p, \alpha\gamma)/(p, \gamma_0)$ over the 323-keV resonance. Top, $(p, \alpha\gamma)/(p, \gamma_0)$; bottom, $(p, \alpha\gamma)/(p, \gamma_1)$. The weighted average ratios and the associated uncertainties are plotted as solid and dashed lines, respectively. Only statistical errors are shown.

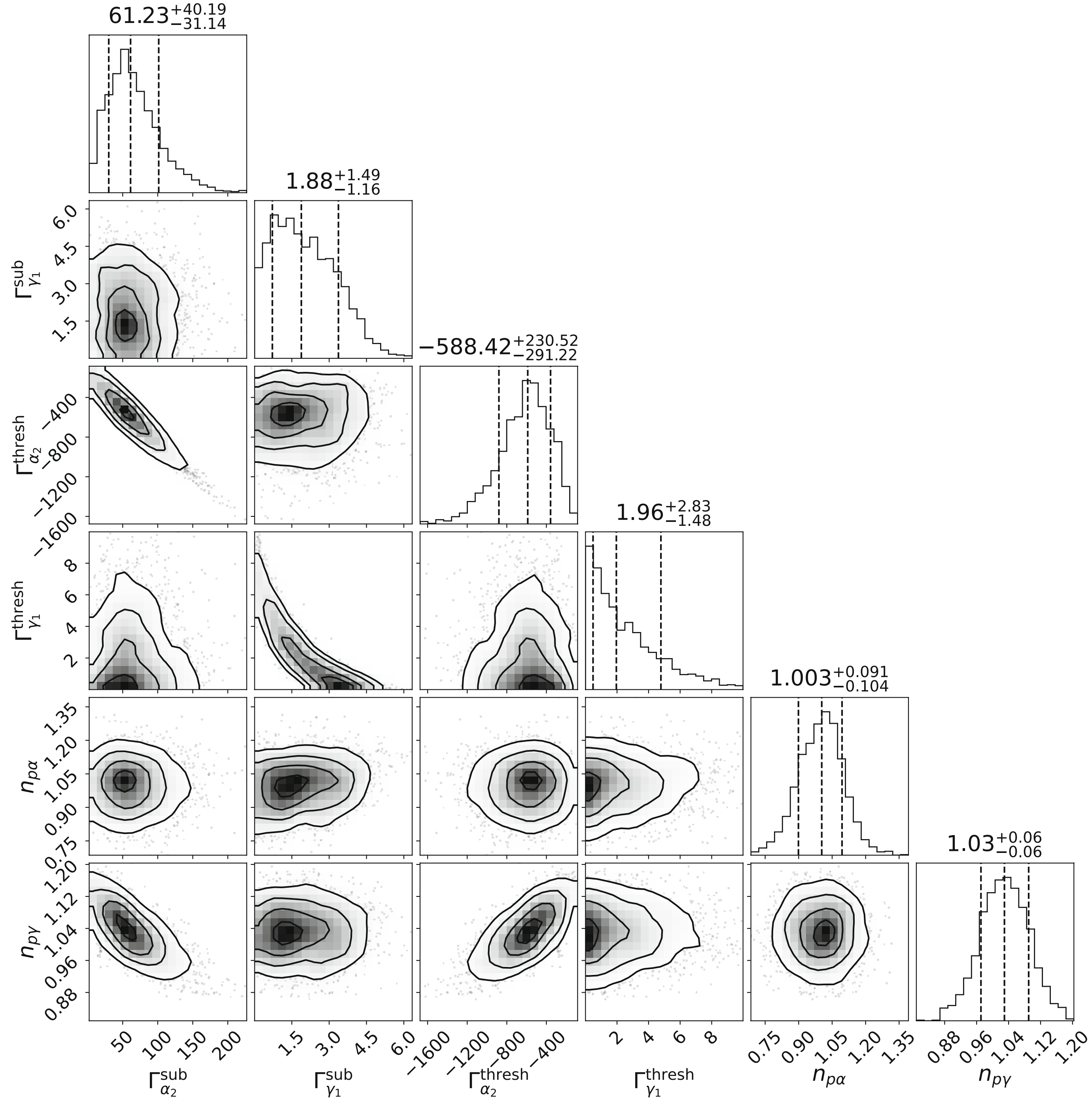

Extended Data Fig. 4 | Corner plot of the covariance matrix for an MCMC analysis of the *R*-matrix fit. The vertical dashed lines indicate 16%, 50% and 84% quantiles. Here 'sub' refers to the sub-threshold state at $E_x = 12.396$ MeV, 'thresh' the near-threshold state at $E_x = 12.855$ MeV, and '$n_{p\alpha}$' and '$n_{p\gamma}$' are the normalization factors for the (p, α) and (p, γ) datasets, respectively. Uniform priors were taken for all parameters of the analysis.

Extended Data Table 1 | Selected astrophysical *S* factors for $^{19}F(p,\gamma)^{20}Ne$ derived in this work

E_{COM} (keV)	S-factor (MeV·b)	Statistical uncertainty (%)
186.4	0.0140(0.0040)	26.1
195.5	0.0132(0.0040)	27.4
252.7	0.0125(0.0018)	8.3
273.8	0.0129(0.0028)	18.3
283.1	0.0262(0.0050)	14.9
291.5	0.0304(0.0047)	9.7

The total uncertainties are listed in the parentheses, and the statistical uncertainties are listed in the last column. Conservatively, we estimate an overall systematic uncertainty of 12%.

Extended Data Table 2 | Thermonuclear reaction rates of ^{19}F(p, γ)^{20}Ne in units of cm^3 s^{-1} mol^{-1}

	Present rate			NACRE (*3*)	deBoer21 (*5*)	Williams21 (*27*)
T_9	Median	Low	High	Median	Median	Median
0.01	1.03×10^{-25}	2.91×10^{-27}	2.05×10^{-25}	4.25×10^{-28}	1.10×10^{-28}	8.17×10^{-28}
0.015	1.30×10^{-21}	8.78×10^{-23}	2.52×10^{-21}	1.37×10^{-23}	3.50×10^{-24}	2.61×10^{-23}
0.02	5.16×10^{-19}	5.80×10^{-20}	9.73×10^{-19}	9.45×10^{-21}	2.38×10^{-21}	1.79×10^{-20}
0.03	9.45×10^{-16}	1.94×10^{-16}	1.70×10^{-15}	3.41×10^{-17}	8.44×10^{-18}	6.45×10^{-17}
0.04	1.08×10^{-13}	3.15×10^{-14}	1.84×10^{-13}	5.95×10^{-15}	1.44×10^{-15}	1.11×10^{-14}
0.05	3.13×10^{-12}	1.16×10^{-12}	5.09×10^{-12}	2.34×10^{-13}	5.57×10^{-14}	4.38×10^{-13}
0.06	4.07×10^{-11}	1.79×10^{-11}	6.33×10^{-11}	3.84×10^{-12}	8.98×10^{-13}	7.19×10^{-12}
0.07	3.15×10^{-10}	1.59×10^{-10}	4.70×10^{-10}	3.60×10^{-11}	8.25×10^{-12}	6.65×10^{-11}
0.08	1.70×10^{-09}	9.57×10^{-10}	2.45×10^{-09}	2.28×10^{-10}	5.15×10^{-11}	4.21×10^{-10}
0.09	7.15×10^{-09}	4.39×10^{-09}	9.91×10^{-09}	1.10×10^{-09}	2.46×10^{-10}	2.02×10^{-09}
0.1	2.53×10^{-08}	1.69×10^{-08}	3.39×10^{-08}	4.31×10^{-09}	9.93×10^{-10}	7.76×10^{-09}
0.15	5.68×10^{-06}	4.86×10^{-06}	6.51×10^{-06}	9.55×10^{-07}	3.36×10^{-07}	1.18×10^{-06}
0.2	2.58×10^{-04}	2.35×10^{-04}	2.84×10^{-04}	8.67×10^{-05}	2.78×10^{-05}	6.92×10^{-05}
0.3	2.18×10^{-02}	1.98×10^{-02}	2.40×10^{-02}	1.93×10^{-02}	5.63×10^{-03}	1.33×10^{-02}
0.4	2.60×10^{-01}	2.37×10^{-01}	2.87×10^{-01}	2.93×10^{-01}	8.99×10^{-02}	1.98×10^{-01}
0.5	$1.31\times10^{+00}$	$1.20\times10^{+00}$	$1.45\times10^{+00}$	$1.63\times10^{+00}$	6.04×10^{-01}	$1.08\times10^{+00}$
0.6	$4.81\times10^{+00}$	$4.39\times10^{+00}$	$5.30\times10^{+00}$	$6.19\times10^{+00}$	$2.90\times10^{+00}$	$4.04\times10^{+00}$
0.7	$1.46\times10^{+01}$	$1.32\times10^{+01}$	$1.60\times10^{+01}$	$1.92\times10^{+01}$	$1.04\times10^{+01}$	$1.22\times10^{+01}$
0.8	$3.73\times10^{+01}$	$3.38\times10^{+01}$	$4.09\times10^{+01}$	$4.88\times10^{+01}$	$2.88\times10^{+01}$	$3.03\times10^{+01}$
0.9	$8.13\times10^{+01}$	$7.41\times10^{+01}$	$8.95\times10^{+01}$	$1.04\times10^{+02}$	$6.41\times10^{+01}$	$6.36\times10^{+01}$
1.0	$1.56\times10^{+02}$	$1.42\times10^{+02}$	$1.72\times10^{+02}$	$1.93\times10^{+02}$	$1.21\times10^{+02}$	$1.17\times10^{+02}$

The rates are for the bare ^{19}F nuclei in the laboratory, that is, no thermally excited target states are considered. Refs.[3,5,27].

Extended Data Table 3 | Calcium yields for fixed trajectory with constant $\rho = 39.8\,\mathrm{g\,cm^{-1}}$, $T = 1.19 \times 10^8$ K and primordial initial composition[42]

^{19}F(p, γ) rate		NACRE ^{19}F(p, α) rate			deBoer ^{19}F(p, α) rate		
		Low	Mean	High	Low	Mean	High
JUNA	Low	-11.59	-11.72	-11.83	-11.70	-11.68	-11.90
	Mean	-11.47	-11.60	-11.70	-11.57	-11.55	-11.77
	High	-11.37	-11.50	-11.60	-11.48	-11.46	-11.67
NACRE	Low	-12.51	-12.64	-12.75	-12.62	-12.60	-12.82
	Mean	-12.21	-12.35	-12.45	-12.32	-12.30	-12.52
	High	-12.04	-12.17	-12.27	-12.15	-12.13	-12.34
deBoer	Low	-13.25	-13.38	-13.48	-13.36	-13.34	-13.55
	Mean	-12.81	-12.94	-13.05	-12.92	-12.90	-13.12
	High	-12.05	-12.18	-12.28	-12.16	-12.13	-12.35
Williams	Low	-12.07	-12.21	-12.31	-12.18	-12.16	-12.38
	Mean	-11.99	-12.13	-12.23	-12.10	-12.08	-12.30
	High	-11.91	-12.04	-12.15	-12.02	-12.00	-12.22

The trajectories were run until the hydrogen mass fraction dropped below 0.01. Other non-degenerate binary reactions are taken from REACLIB v2.2. The reference rate for just using the original REACLIB rates for all binary reactions gives a mass fraction of log(^{40}Ca)=−12.33. Values are given in logarithm base 10.

Extended Data Table 4 | Similar to Extended Data Table 3 but uses the actual central temperature trajectory of a 40 $M_\odot$ population III star model[2] and using a mixing model to emulate convection

^{19}F(p,γ) rate		NACRE ^{19}F(p,α) rate			deBoer ^{19}F(p,α) rate		
		Low	Mean	High	Low	Mean	High
JUNA	Low	-11.29	-11.44	-11.54	-11.36	-11.41	-11.66
	Mean	-11.14	-11.29	-11.39	-11.22	-11.26	-11.51
	High	-11.03	-11.18	-11.29	-11.11	-11.15	-11.41
NACRE	Low	-12.19	-12.33	-12.44	-12.26	-12.31	-12.56
	Mean	-11.89	-12.04	-12.14	-11.97	-12.01	-12.26
	High	-11.72	-11.86	-11.97	-11.79	-11.83	-12.09
deBoer	Low	-13.13	-13.27	-13.38	-13.20	-13.24	-13.49
	Mean	-12.52	-12.66	-12.77	-12.59	-12.63	-12.89
	High	-11.72	-11.86	-11.97	-11.79	-11.83	-12.09
Williams	Low	-11.74	-11.88	-11.99	-11.81	-11.85	-12.11
	Mean	-11.66	-11.80	-11.91	-11.73	-11.77	-12.03
	High	-11.57	-11.71	-11.82	-11.64	-11.69	-11.94

The trajectory was run until a core hydrogen mass fraction of 0.01. The mixing model assumes that the trajectory represents a fraction of $\tau_{\mathrm{mix}}=0.0595$ of the total reservoir such that burning reduced the H mass fraction in the trajectory to 0.01, consistent with the stellar model. The reference rate for just using the original REACLIB rates for all binary reactions is log(^{40}Ca) = −12.02.

Extended Data Table 5 | Calcium yields for full stellar models

^{19}F(p,γ) rate		^{19}F(p,α) rate		TAMS	Pre-supernova		
				Star	H envel.	He shell	H+He envel.
JUNA	Low	NACRE	High	-10.81	-11.18	-10.74	-11.13
	Mean		Mean	-11.10	-11.47	-11.05	-11.41
	High		Low	-11.41	-11.77	-11.39	-11.73
NACRE	Low	NACRE	High	-11.56	-11.93	-11.51	-11.88
	Mean		Mean	-11.90	-12.27	-11.86	-12.21
	High		Low	-12.31	-12.68	-12.25	-12.63
deBoer	Low	NACRE	High	-11.56	-11.92	-11.49	-11.88
	Mean		Mean	-12.51	-12.88	-12.46	-12.85
	High		Low	-13.62	-13.98	-13.57	-13.94
Williams	Low	NACRE	High	-11.40	-11.77	-11.39	-11.73
	Mean		Mean	-11.64	-12.01	-11.62	-11.96
	High		Low	-11.83	-12.20	-11.83	-12.16

The first data column gives the average abundance over the entire star at the terminal-age main-sequence (TAMS), defined by a core hydrogen mass fraction of 0.01, consistent with what we use elsewhere. The last three columns list the average calcium mass fraction at the pre-supernova stage: in the hydrogen envelope (hydrogen mass fraction ≥0.01), in the helium shell (helium mass fraction ≥0.01 and hydrogen mass fraction <0.01), and in the combination of both (helium mass fraction ≥0.01), respectively. Values are given in logarithm base 10.